



# An investigation of spatial variation of suspended sediment concentration induced by a bay bridge based on Landsat TM and OLI data

LiNa Cai<sup>a,b,c</sup>, DanLing Tang<sup>a,c,\*</sup>, CongYing Li<sup>d</sup>

<sup>a</sup> *Research Center for Remote Sensing of Marine Ecology & Environment, State Key Laboratory of Tropical Oceanography, South China Sea Institute of Oceanology, Chinese Academy of Sciences, Guangzhou 510301, China*

<sup>b</sup> *Zhejiang Ocean University, Zhoushan, Zhejiang 316004, China*

<sup>c</sup> *University of Chinese Academy of Sciences, Beijing 100049, China*

<sup>d</sup> *Naval Aeronautical and Astronautical University, Yantai 264001, China*

Received 30 August 2014; received in revised form 6 April 2015; accepted 13 April 2015

Available online 21 April 2015

## Abstract

This study investigates the spatial variation of suspended sediment concentration (SSC) induced by Hangzhou Bay Bridge (HBB) in the coastal waters of the East China Sea. Based on Landsat Thematic Mapper (TM), Operational Land Imager (OLI) data and in-situ measurements, spectral characteristics of waters in Hangzhou Bay and SSC retrieved from near infrared single band have been analyzed. The results revealed significant difference of SSC in the water on two sides of HBB. SSC increases downstream of the bridge under conditions of low turbidity ( $SSC < 300 \text{ mg l}^{-1}$ ) upstream water, while SSC decreases when high turbidity water ( $SSC > 400 \text{ mg l}^{-1}$ ) upstream. This study shows that the interaction of bridge piers and currents has important influences on SSC distribution by inducing hydrodynamic factors and by changing suspended sediment transport. Remotely sensed data with high spatial resolution as TM and OLI can be applied to investigate SSC variations induced by a bridge in the bay area.

© 2015 COSPAR. Published by Elsevier Ltd. All rights reserved.

**Keywords:** Remote sensing; Bay bridge; Suspended sediment concentration; Variation

## 1. Introduction

Many big constructions have been built in coastal waters in recent years. Prior studies found that these constructions affect the surrounding water flow dynamics, e.g. horseshoe vortex systems could be induced by bridge piers (Unger and Hager, 2007), the current velocity will

be influenced by bridges (Qiao et al., 2011) and local scour has been found around bridge piers (Baban, 1997; Baker, 1979; Pasiok and Stilger-SzydŁO, 2010; Ting et al., 2001). However, it is unclear whether such offshore construction has any impacts on water quality, and how it affects suspended sediment concentration (SSC) in the water nearby. In this paper, using satellite and in-situ data, we investigate the impacts of a bay bridge on the distribution of SSC.

Suspended sediment is one of the key factors of the ocean environment. It is a significant carrier of carbon, nutrients, pollutants and other material (Ilyina et al., 2006; Mayer et al., 1998; Webster and Lemckert, 2002;

\* Corresponding author at: South China Sea Institute of Oceanography, Chinese Academy of Sciences, 164 Xingang Xi Road, Guangzhou 510301, China. Tel./fax: +86 20 89023203.

E-mail address: [lingzistdl@126.com](mailto:lingzistdl@126.com) (D. Tang).

URL: <http://lingzis.51.net/> (D. Tang).

Yan and Tang, 2009). The Yangtze River is the fourth largest sediment loaded river in the world. With more than 400 million tons per year (Chen et al., 2003), it carries a lot of sediments to the Hangzhou Bay. Those suspended sediments significantly influence the ecology, geomorphological evolution, and the water quality of Hangzhou Bay.

MERIS and Coastal Zone Color Scanner (CZCS) data have been applied to track the suspended sediment concentration (SSC) and pigment concentration in the coastal waters of China (Shen et al., 2010; Tang et al., 1998), and recently, MODIS data showed the northward drift of SSC in the Yangtze estuary in spring (Zhang et al., 2014b). The spatial resolution of most satellite data (SeaWiFS, MODIS, MERIS and GOCI) is of the order of a few hundred meters, and is too low to estimate the effects of bridges on the local water quality environment. Therefore, we need high spatial resolution satellite data and corresponding methods for local water area research.

With high spatial resolution (dozens of meters), Landsat TM and ETM + data, SPOT (Satellite Pour l'Observation de la Terre, or "Earth observation satellite") data, and ASTER (Advanced Spaceborne Thermal Emission and Reflection Radiometer) can clearly delineate the changes in water bodies in bay areas (Charou et al., 2010). The visible and near infrared bands of Landsat TM and ETM + images were used to retrieve SSC for the Yellow River estuary (Fan et al., 2007; Zhang et al., 2014a). Using Landsat TM4 band, suspended particulate matter concentration was retrieved from a low SSC river (Onderka and Pekárová, 2008). An estimation model of SSC in Yangtze River was built based on spectral analysis (Chen et al., 2005) and the relationship between spectral volume reflectance and suspended sediment was studied based on upwelling multispectral radiance (Bukata et al., 1988). Studies on the influence of suspended sediment particles on the water reflectance spectrum (Doxaran et al., 2006; Qiu, 2013; Wang et al., 2012; Zhou et al., 2006) found close relationships between SSC and the band ratio (NIR/blue, red/green, NIR/red), and between the total suspended matter and the red band. The near infrared band was found to be sensitive to SSC in suspended sediment (SS) dominated water (Dekker et al., 2002). Currently, remote sensing methods to detect SSC variations induced by big nearshore constructions are under development. Can we apply relatively high spatial resolution Landsat Thematic Mapper (TM), Operational Land Imager (OLI) (T-O) data to observe the effects of bay bridges on SSC in coastal waters?

In this study, taking the advantage of high spatial resolution data from Landsat (T-O), we analyzed the spectral characteristics of waters in the study area, conducted water unsupervised classification, and estimated SSC around the bridge. We aim to determine how to employ remote sensing to reveal spatial variation of SSC affected by Hangzhou Bay Bridge (HBB).

## 2. Data and method

### 2.1. Study area and Hangzhou Bay Bridge (HBB)

Hangzhou Bay is located in the East China Sea, between 29°–32°N and 120°–123°E (Fig. 1(A) and (B)) with an area of approximately 8500 km<sup>2</sup>. Its average depth at low tide is 8–10 m (Liu et al., 2012; Wang et al., 2012; Xie et al., 2009), with a tidal amplitude of 9 m at the head of Hangzhou Bay, 4–6 m further downstream and 3–4 m at the mouth (Lin et al., 2005; Xie et al., 2009).

The HBB (Fig. 1(C) and (D)) is a large bridge with a length of about 36 km. It spans the main channel of Hangzhou Bay and connects the municipalities of JiaXing and Ningbo Cixi in Zhejiang province. It was built in 2003 and has been operating since 2007.

### 2.2. In-situ data

In order to determine the spectral characteristics of the water containing suspended sediment in Hangzhou Bay, we ran a spectral analysis of in situ data and built a SSC retrieval model. The surveys were conducted in Hangzhou Bay (from 9:00 a.m. to 4:00 p.m.) on 23 July 2011 and on 30 March 2014. Sampling stations covered one area between 30.2°–30.5°N and 121.5°–121.62°E (S<sub>1</sub> in Fig. 1(B)), and a second area between 29.91°–29.98°N and 122.17°–122.22°E (S<sub>2</sub> in Fig. 1(B)).

In the survey on 23 July 2011, 75 water samples were collected during 9:45–10:45 a.m. to establish and validate the model based on the synchronously obtained satellite data. Eight fishing boats were distributed evenly in Fig. 1(S<sub>1</sub>). These boats changed their places and sampled with an interval of 200–500 m. The SSCs were retrieved from water samples in laboratory. During 11:00 a.m.–4:00 p.m., the SSCs and remote sensing reflectance (Rrs) were synchronously measured using a boat at four stations in Fig. 1(S<sub>1</sub>).

In the survey on 30 March 2014, the SSCs (water samples) and Rrs at four stations in Fig. 1(S<sub>2</sub>) were obtained from 9:00 a.m. to 4:00 p.m..

Furthermore, a set of experimental data was retrieved from an open-air ocean water pool. The SSC was low in this pool because of longtime deposition. The SSC and the remote sensing reflectance (Rrs) were measured strictly following the NASA SIMBIOS ocean optics protocols (Mueller et al., 2003).

The Rrs was detected by an ISI921VF visible, near infrared (NIR), high spectral radiometer and an ASD FieldSpec Dual VNIR, with 380–1080 and 350–1050 nm spectral range respectively. We performed an absolute radiance calibration of the detectors before measurement. Using a 3 m long hand-held pole, the optical fiber tip was kept 1 m above the water surface during the measurements. Using a hand-held pole with adjustable-angle equipment, the viewing angles for the above-water measurement can be controlled so that the zenith and azimuth are

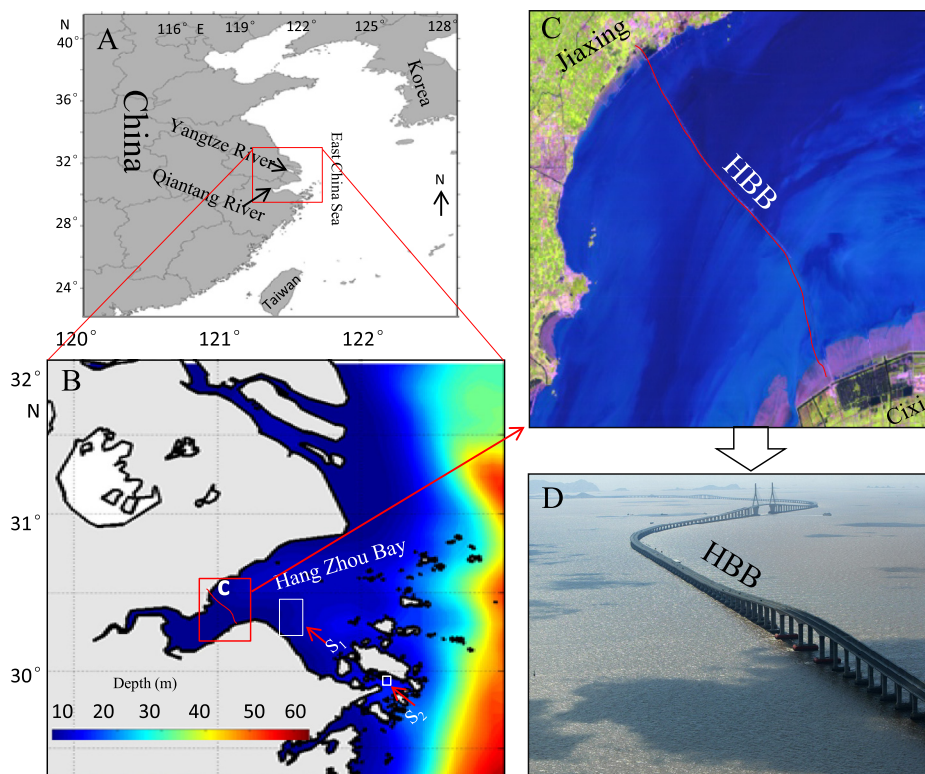


Fig. 1. (A) Location of Hangzhou Bay. (B) Bathymetry of Hangzhou Bay. (C) Location of HBB on false color image (composed from TM bands 5, 4 and 3). (D) Photo of HBB. (S<sub>1</sub>–S<sub>2</sub>) Location of two in situ sampling areas.

approximately 40° and 135° (Qiu, 2013; Wang et al., 2012), respectively. The measurement locations were selected to minimize interference from shading, boat superstructure reflections, ship wakes, surface foam patches and whitecaps. Additionally, the location was also selected so that it was easy to point towards a direction away from the sun glint.

The measured  $R_{rs}$  is calculated from Eq. (1):

$$R_{rs} = \frac{L_s - \rho L_{sky}}{\pi L_p / \rho_p} \quad (1)$$

where  $L_s$  is the radiance received by the ISI921VF/ASD above the sea water surface;  $L_{sky}$  is the radiance of the sky, it can be measured pointing the radiance sensor towards the sky with an angle of 40° to the zenith and an azimuth angle of 135°;  $\rho_p$  is the reflectance of the plate;  $L_p$  is the radiance received by the ISI921VF/ASD above the plate.  $\rho$  is the dimensionless air–water reflectance and is always in the range of 0.022–0.05,  $\rho$  is calculated with the assumption of a black ocean at wavelengths from 1000 to 1020 nm (Hale and Querry, 1973) and wavelength-independent (Doxaran et al., 2002). When  $\rho$  is out of the range of 0.022–0.05, it is determined from the sea conditions (Lee et al., 1996; Mobley, 1999; Tang et al., 2004).

The SSC, defined as the dry mass of particles per unit volume of water (units are  $\text{mg l}^{-1}$ ), was determined following the steps of Qiu (2013). Using 10-liter Niskin bottles,

the water samples were taken, simultaneously with in situ optical measurements, just below the sea surface. To filter the water samples, a 0.45  $\mu\text{m}$  filter (Whatman GF/F filters) and vacuum filtration system were prepared. The SSCs were obtained after the filters have been dried for 24 h at 40 °C and reweighed. An electronic analytic scale was used to weigh the dry-weight of the filter-pad. The blank filter and sampled filter-pad were weighed until the difference between two successive SSC calculated from the scale reading was less than 0.01  $\text{mg l}^{-1}$ .

### 2.3. Satellite data

Landsat-5 Thematic Mapper (TM) and Landsat-8 Operational Land Imager (OLI) images were chosen to analyze the changes in water quality. The wavelength used in the TM sensor was from 0.45 to 12.50  $\mu\text{m}$ . Six spectral bands (spatial resolution of 30 m) of TM are shown in Table 1, where the thermal infrared band is not included. OLI includes nine bands (Table 1) with spatial resolution of 30 m for eight bands and 15 m for one panchromatic band (0.50–0.68  $\mu\text{m}$ ). Seven Landsat-5 TM images retrieved at around 10:15 a.m. and six Landsat-8 OLI images acquired at around 10:25 a.m. were studied in this paper.

To show the bridge's effects on water environment, unsupervised classification was conducted on both OLI (six OLI images) and TM (seven TM images) data. To

Table 1  
Bands information and image acquired date.

OLI			TM		
Number	Bands ( $\mu\text{m}$ )	Acquired date	Number	Bands ( $\mu\text{m}$ )	Acquired date
1	0.433–0.453	12 Jul. 2013			2 Jul. 2007
2	0.450–0.515	13 Aug. 2013	1	0.450–0.515	28 Jul. 2007
3	0.525–0.600	29 Aug. 2013	2	0.525–0.605	24 Mar. 2008
4	0.630–0.680	17 Nov. 2013	3	0.630–0.690	11 May 2008
5	0.845–0.885	03 Dec. 2013	4	0.775–0.900	17 Jul. 2009
6	1.560–1.660	13 Jun. 2014	5	1.550–1.750	9 Nov. 2010
7	2.100–2.300		7	2.090–2.350	23 Jul. 2011
8	0.500–0.680				
9	1.360–1.390				

further show the details of SSC variations on two sides of the bridge, as examples, SSC was derived from seven TM images. The images used in this paper were chosen in clear sky conditions. The satellite data acquired dates were shown in Table 1.

#### 2.4. Data analysis

Atmospheric correction is needed to eliminate the influence of the atmospheric effects before retrieving SSC from satellite data. We conducted relative atmospheric correction by employing a dark pixel subtraction method (Chavez, 1988; LU et al., 2002; Mustak, 2013). This atmospheric correction method is based on the theory that, dark objects reflect no light, any value greater than zero must result from atmospheric scattering. In our study, land-based clear water bodies (such as clear lake waters) were used as standard reflectors for atmospheric measurements. The reflectance contributed by the atmosphere in each band was assumed to be the difference between the apparent reflectance and the surface reflectance of clear lake water (dark object), whose surface reflectance in TM bands 1–5 and 7 is approximately equal to 0.04, 0.05, 0.03, 0.01, 0.01 and 0.01, respectively (Richter, 1990; Teillet and Fedosejevs, 1995). The scattering contributed by atmosphere can be removed by subtracting this value from every pixel in each band individually (Chavez, 1988; Tyagi and Bhosle, 2011). In our study, the comparative analysis is conducted between two sides of the bridge on each single image separately and therefore relative atmospheric correction can meet our requirements (Lavender et al., 2005; Onderka and Pekárová, 2008). The clear lake water (dark pixels) can be found in the entire image containing the study area or in adjacent images in the same orbit.

To convert the digital data to radiance at the sensor, the calibration was carried out using the formula of Onderka and Pekárová (2008) and listed in Eq. (2) below.

$$L_{\lambda} = Bias_{\lambda} + Gain_{\lambda} \times DN_{\lambda} \quad (2)$$

$L_{\lambda}$ : the radiance at the sensor in units of  $\text{Wm}^{-2} \text{sr}^{-1} \mu\text{m}^{-1}$ ,  
 $Bias_{\lambda}$  and  $Gain_{\lambda}$ : the bias and gains for the  $\lambda$  wavelength band,

$DN_{\lambda}$ : the original pixel value (Li et al., 2010; Onderka and Pekárová, 2008).

The spectral profile curves were retrieved from Landsat Thematic Mapper (TM) and Operational Land Imager (OLI) (T-O) multispectral images to analyze the spectral difference of the water in the vicinity of the bridge. Unsupervised classification was performed using the ISODATA (Iterative Self-Organizing Data Analysis Techniques Algorithm) (Ball and Hall, 1965; Irvin et al., 1997; Li et al., 2006). The process of unsupervised classification performs searching in multispectral image and defines clusters of similar spectral characteristics with limited initial input and without need to manually select a training sample. The clusters are formed automatically according to pixel spectrum and spatial characteristics. Water spectral features, which are mainly determined by the absorption and scattering effects of suspended substances, reflect the integrated water constituent information. The pixels of the same water constituents have the same values in every band and cluster together as one class.

To reveal the details of SSC variation in the vicinity of the bridge, we built a SSC retrieval model, using NIR single band, to retrieve SSC from Landsat-5 TM images. A minimum of eight pixels are around the pixel where the in-situ data locates. We selected four (on the up, down, left and right side of the central pixel), with an interval of one pixel, from the eight pixels around. Together with one central pixel, five pixel values (i.e. the radiances in  $TM4 - L(TM4)$ ) around each sampling site were first averaged and then used for calibration. The logarithmic relationship between the averaged  $L(TM4)$  radiances and actual SSC was found (Eq. (3), with  $R^2$  0.951 and  $P < 0.001$ ) using the calibration data set. The data set contain 35 in-situ samples. The SSC values of water samples range from 203 to 481  $\text{mg l}^{-1}$ , with a mean value of 350  $\text{mg l}^{-1}$ .

$$\ln(SSC) = 0.01113115 \times L(TM4) + 4.7942296 \quad (3)$$

SSC: The suspended sediment concentration ( $\text{mg l}^{-1}$ ),

$L(TM4)$ : The radiance in the near infrared band (calibrated after Eq. (2) and atmosphere correction).

All calculations were performed with the processing software ENVI (4.5 and 5.1) following the relevant guidelines (ENVI, 1997).

### 3. Results

#### 3.1. Spectral characteristics changing trend and correlation with SSC

Low SSC (SSC less than  $100 \text{ mg l}^{-1}$ ) water spectral curves in experimental data show two reflectance peaks (Fig. 2(A)): a primary one and a secondary one. The major peak appears in the range of 500–600 nm, while the weak one is around 800 nm. For high SSC (more than  $150 \text{ mg l}^{-1}$ ) water, in-situ measurement data (Fig. 2(B) and (C)) shows that the first reflectance peak moves rightward and appears in the range of 590–730 nm, while the second one remains at around 800 nm with its intensity becoming similar to that or stronger than the first one. Two reflectance peaks (double peaks) of high SSC water indicate a strong reflection of SS in these two bands, and also that red and NIR bands are sensitive to the change in SSC. In general, the intensity of reflectance peak increases significantly with the increase of SSC in NIR band for relatively high SSC water (Fig. 2(B) and (C)). The spectral curve of a in Fig. 2(C),

whose SSC was  $799 \text{ mg l}^{-1}$ , sampled from the area  $S_2$  shown in Fig. 1(B), has the highest reflectance peaks in red and NIR bands. The lowest SSC ( $470 \text{ mg l}^{-1}$ ) sampled from the area  $S_1$  in Fig. 1(B) has the lowest reflectance peaks in the two bands (curve d in Fig. 2(C)). The intensity of reflectance peaks in red and NIR bands for curve c in Fig. 2(C) is moderate, with SSC of  $513 \text{ mg l}^{-1}$ . There also exist plot excursions in the short wavelength (Fig. 2), indicating that the water-leaving signal is not determined entirely by suspended matter, even in this kind of high particle concentration waters.

The correlation analysis between SSC and Rrs at different wavelengths (Table 2) shows: among all the bands in the range of 350–1080 nm, the near infrared band indicates the highest correlation coefficient ( $R$ : 0.836) between SSC and Rrs (averaged of 852.56 and 880.4 nm). The red band presents a secondary peak correlation coefficient ( $R$ : 0.71) with the SSC (averaged of 666.07 and 688.34 nm). The relevant parameters are shown in Table 2.

#### 3.2. Different spectral profile curves and water classes on two sides of the bridge

We denoted the difference of water spectral profiles by showing spectral values in various bands of TM images (Fig. 3(A1–C1)) and OLI images (Fig. 3(D1–F1)). The

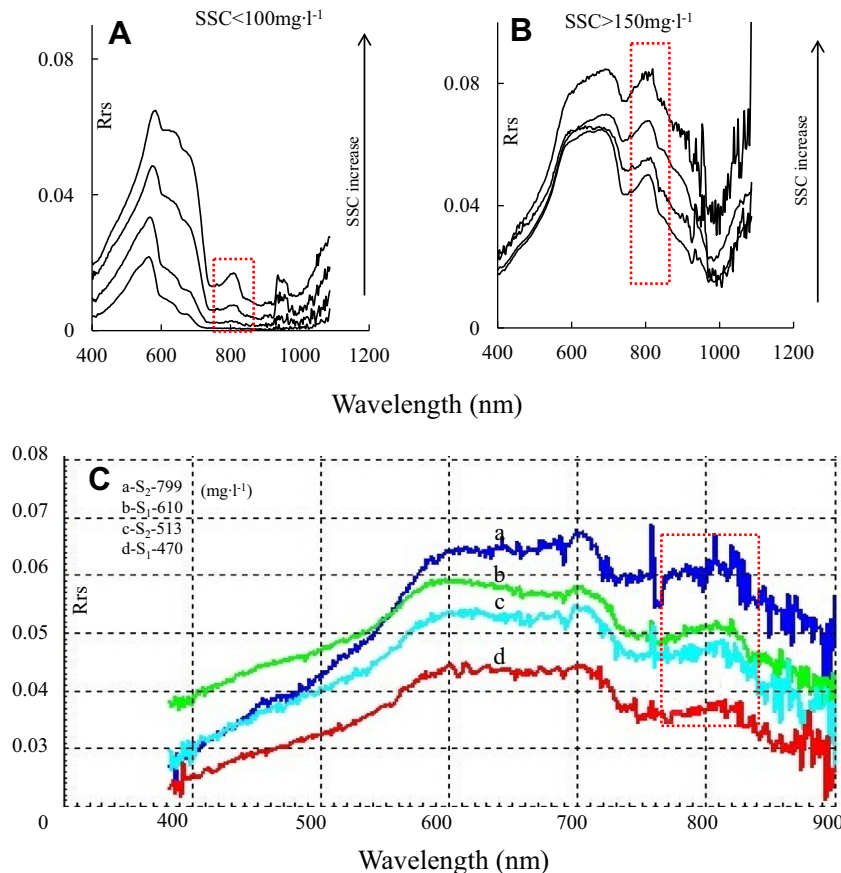


Fig. 2. (A) Experimentally measured water spectral reflectance curves of low SSC water ( $SSC < 100 \text{ mg l}^{-1}$ ). (B and C) In situ measured water spectral reflectance curves sampled from Fig. 1 ( $S_1$ – $S_2$ ) in Hangzhou Bay.

Table 2  
Eigenvalues of correlation analysis between SSC and Rrs at different wavelengths.

Wavelength <sup>a</sup> (nm)	SSC				
	R	R <sup>2</sup>	$\bar{R}^2$	Sig (P)	F
410.35 <sup>B</sup>	0.687	0.472	0.428	0.007	10.727
501.98 <sup>B</sup>	0.559	0.313	0.255	0.038	5.457
548.48 <sup>G</sup>	0.549	0.302	0.243	0.042	5.182
604.83 <sup>G</sup>	0.674	0.454	0.409	0.008	9.997
666.07 <sup>R</sup>	0.705	0.497	0.455	0.005	11.863
688.34 <sup>R</sup>	0.715	0.526	0.486	0.003	13.29
852.56 <sup>N</sup>	0.830	0.690	0.664	0.000	26.676
880.40 <sup>N</sup>	0.841	0.707	0.682	0.000	28.928

<sup>a</sup> B-Blue, G-Green, R-Red, N-Near infrared.

selected paired points (two pairs for each image) are marked on the images (Fig. 3(A)–(F)). Two sides of the bridge, the upstream (Up) and downstream (Dw) were defined according to the pier induced flow (pier wake) and the position relative to the bridge. The pier induced flow can be interpreted from Landsat enhanced color images. The examples were shown in Fig. 3(P1, P2). We defined the pier wake side as downstream, thus the opposite side of the bridge is upstream.

The difference in pixel values of the paired points was used to describe the spectral variation in the water on two sides of the bridge. Here we assume that the variations of the atmospheric optical characteristics over the small area associated with a bridge can be ignored. As a result, the difference in pixel values between the paired points is mainly due to the difference in water spectral characteristics.

Spectral curves and values are obviously different on opposite sides of HBB. This is especially the case in the NIR band as is shown in red dotted line frames in Fig. 3(A1–F1). The spectral values of NIR band on the downstream side of the HBB change, becoming larger or smaller than those on the upstream side, shown in Table 3.

Two-dimensional spectral feature spaces have been retrieved from the TM image on 28 July 2007 and OLI image on 03 December 2013 (Fig. 4(A)). The candlelight shaped parts in the white circles for TM (red color parts in black circles for OLI) represent sea water. Different positions in the circled area represent different level of water constituents (Fig. 4(A)).

Based on the spectral feature space, sea water of the study area can be divided into seven classes (Fig. 4(B)). For example, two TM images and two OLI images show distributions of different class waters. An obvious difference in water class, highlighted by black circles in Fig. 4(B), is found on opposite sides of the bridge. Near the middle of the HBB, the water is classified to be class 3 on one side (panel a in Fig. 4(B)) and class 5 and 6 on the other side. Furthermore, similar water class patterns, i.e. different water classes on two sides of the bridge, can be observed from OLI images c and d in Fig. 4(B).

### 3.3. Variation of SSC on two sides of the bridge

TM retrieved SSC and the examples taken on 23 July 2011 and 28 July 2007 were shown in Fig. 5(A) and (B). SSC is higher on the northwest and south sides of the bridge than that near the center of the HBB. The maximum SSC in the study area is nearly 750 mg l<sup>-1</sup>, with the average SSC around 300 mg l<sup>-1</sup>. These levels suggest high turbidity in the research area. In addition, the data shows distinctly different distributions of SSC on opposite sides of the bridge.

Additionally, thirty paired sub-areas were sampled (on the image) on opposite sides of the bridge with each sub-area being 0.81 km<sup>2</sup> in area. Each pair lied symmetrically on opposite sides of the bridge and distributed as consistent as possible with the current direction. Statistical analysis of SSC values was conducted on every sub-area (examples are shown Fig. 5(B) and Table 4). The SSC in upstream sub-area d in Fig. 5(B) is in the range of 212–227 mg l<sup>-1</sup> (Fig. 5(D)), lower than that of downstream sub-area c whose SSC ranged in 255–282 mg l<sup>-1</sup> (Fig. 5(C)). The SSC of upstream sub-area B (mean value 176 mg l<sup>-1</sup>) is clearly lower than that of downstream sub-area A (mean value 260 mg l<sup>-1</sup>) (Table 4). The same pattern is also observed across sampled pairs D and C, J and I in Table 4. The SSC increases in value of 35 and 68 mg l<sup>-1</sup> from upstream to downstream. However, SSC declines downstream in some paired sub-areas. For example, SSC decreases across upstream samples F, H and L, N compared to their downstream pairs E, G, K and M (Table 4). SSC does not change much from sub-area P to O. Similar change trends can be observed in other paired sub-areas.

Based on the analysis of all sampling sub-areas, we found that SSC increases significantly downstream under the condition of low turbidity water (SSC less than 300 mg l<sup>-1</sup>) upstream. However, if high turbidity (SSC more than 350 mg l<sup>-1</sup>) upstream, SSC can also increase downstream, but the frequency of increase is lower; SSC often decreases downstream especially when SSC more than 400 mg l<sup>-1</sup> upstream. SSC remains unchanged downstream occasionally.

The comparative analysis was conducted between the model estimated SSC and the values of spectral profile curves at NIR band in Fig. 3(A1–F1). Comparing the coupled points in Fig. 3(A)–(F) showed that the trend of changes in SSCs is the same as their spectral variations' trend at NIR band (Table 3).

## 4. Discussion

### 4.1. The feasibility of SSC inversion model

The novelty of this new build SSC retrieval model is: Logarithmic algorithm was built using NIR single band, and was firstly used in coastal waters. This is because in SSC dominant water, NIR band is most sensitive to SSC among all the wave bands (blue, green, red and NIR bands).

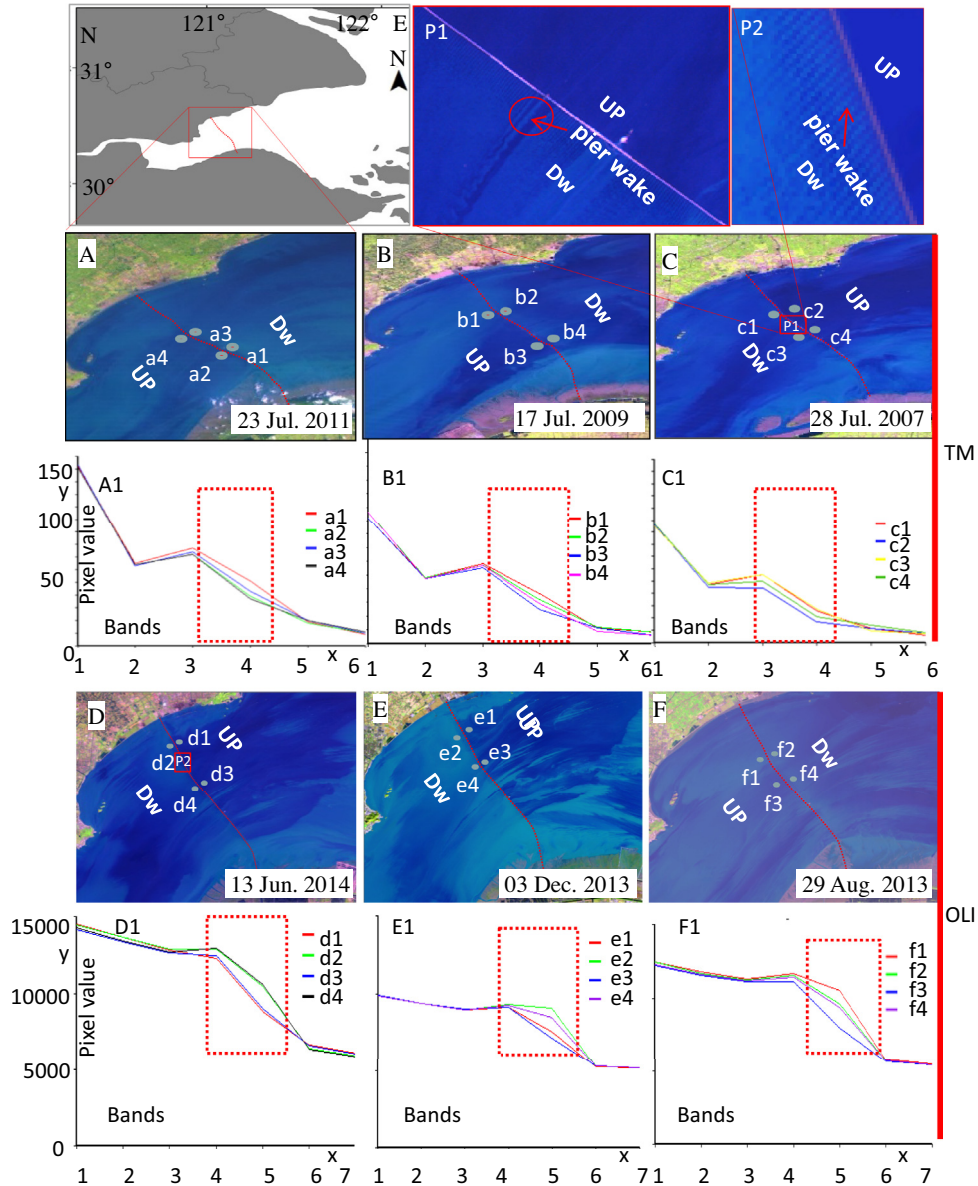


Fig. 3. Comparison of spectral profile curves between paired sampling points. TM: Thematic Mapper data. (A–C) False color image composed from TM bands 5, 4 and 3. OLI: Operational Land Imager data. (D–F) False color image composed from OLI bands 6, 5 and 4. (a1–a4, b1–b4, c1–c4, d1–d4, e1–e4, f1–f4) Sampling points in images (A–F) and corresponding spectral profile curves in panels (A1–F1). *x*-axis in panels (A1–C1): Bands number of TM containing six bands, i.e. bands 1–5 and band 7 (band 7 was numbered 6). *x*-axis in panels (D1–F1): Bands number of OLI containing seven bands, i.e. bands 1–7. *y*-axis in panels (A1–F1): Pixel value. (P1–P2) Bridge pier wake. Up: Upstream; Dw: Downstream.

Our in situ measurements of water spectral characteristics (Fig. 2(B) and (C)) are consistent with a previous study in Hangzhou Bay (Wang et al., 2012), and also consistent with measurements of high SSC water from the Yellow River Estuary (Qiu, 2013). Other studies also showed the same typical spectral characteristics in high turbidity water (Curran and Novo, 1988; Doxaran et al., 2006; Zhang et al., 2010). Those water spectral curves indicate that Hangzhou Bay is dominated by suspended sediment (Wang et al., 2012; Zhang et al., 2010). In a prior study, using a single NIR band (TM4), suspended particulate matter concentration was retrieved in the river (Onderka and Pekárová, 2008). In this paper, the model was built,

using NIR band, to retrieve SSC in the bay area coastal waters.

Table 3  
Water spectral value changing trend from upstream (Up) to downstream (Dw) at NIR band.

Up	Change	Dw	Up	Change	Dw
a2	<	a1	d1	<	d2
a4	<	a3	d3	<	d4
b1	>	b2	e1	<	e2
b3	<	b4	e3	<	e4
c2	<	c1	f1	>	f2
c4	<	c3	f3	<	f4

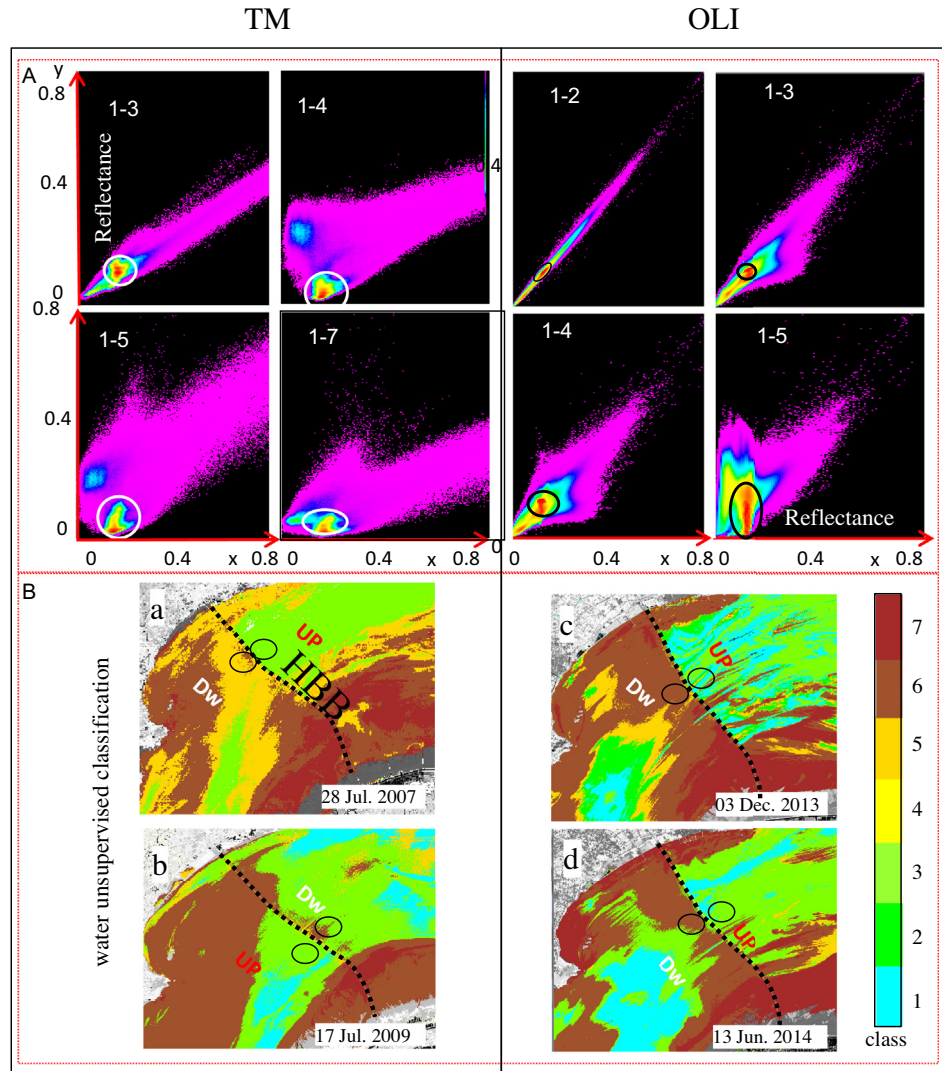


Fig. 4. (A) Two-dimensional spectral feature space of corresponding two bands. Arabic numerals in each block: The bands that constitute the spectral space; First band number:  $x$ -axis; Second number:  $y$ -axis. Candlelight shaped parts in circles: Seawater spectral feature space. TM: Thematic Mapper data. OLI: Operational Land Imager data. (B) Results of water unsupervised classification derived from Landsat TM (a–b) and OLI (c–d) images. (a–d) The same location as Fig. 1C. Black dotted line: HBB.

The distribution of model estimated SSC in this study (take image on July 28, 2007 as example) is consistent with the SSC in a previous research (Li et al., 2010). They all showed the lowest SSC in the northeast of the bridge (around  $200 \text{ mg l}^{-1}$ ), the medium SSC (around  $370 \text{ mg l}^{-1}$ ) in the west of HBB and the highest SSC (around  $700 \text{ mg l}^{-1}$ ) in the south part of the bridge. Meanwhile, comparative analysis was conducted using a TM image (23 July 2011) and a validation data set of 40 samples sampled at around 10:15 a.m. (very close to the acquired time of the TM image) from  $S_1$  in (Fig. 1(B)) on 23 July 2011. The linear regression coefficient of determination of modeled results and measured SSC,  $R^2$ , is 0.979 (Fig. 6).

Furthermore, in this paper, comparative analysis of SSC was conducted on both sides of the bridge in every single image. What we need to know is the relative change trend of SSC on opposite sides of the bridge, i.e. is there a relative

increase or decrease in SSC, or does it remain unchanged? The model estimated SSC using the regression algorithm confirms that it is suitable to conduct single image comparative analysis between two sides of a bridge.

#### 4.2. SSC variation induces different water classes on two sides of the bridge

The results of unsupervised classification using Landsat T-O data showed obviously different water masses in the vicinity of the bridge. Spectral profile curves and values retrieved from the same area corresponding to different water masses mentioned above were clearly different in NIR band.

The water in Hangzhou Bay is dominated by suspended sediment (Wang et al., 2012; Zhang et al., 2010), our

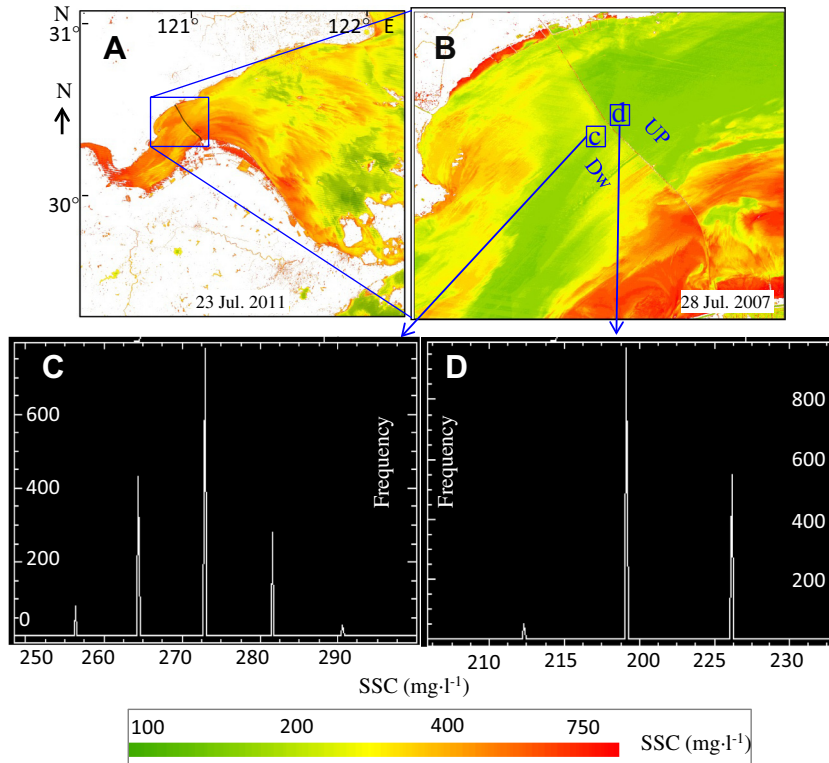


Fig. 5. Sea surface SSC derived from Landsat TM images. (A) SSC on 23 July 2011. (B) SSC on 28 July 2007. (C–D) Histogram of SSC in each corresponding sub-area (c–d) in sub-figure (B). Black dotted line: HBB.

Table 4  
SSC ( $\text{mg}\cdot\text{l}^{-1}$ ) changing trend from upstream (Up) to downstream (Dw).

Up (SSC)	Change	Dw (SSC)	Up (SSC)	Change	Dw (SSC)
B (176)	<	A (260)	J (267)	<	I (335)
D (285)	<	C (320)	L (404)	>	K (361)
F (400)	>	E (375)	N (475)	>	M (438)
H (481)	>	G (427)	P (412)	=	O (410)

analysis of in-situ SSC and Rrs showed that NIR band is the band most sensitive to SSC in SS dominant water.

Furthermore, the distribution of SSC is consistent with the results of water classification, i.e. the water with the same or similar SSC (Fig. 5(B)) was classified into the same class (panel a in Fig. 4(B)). Different water classes corresponded to the changes in SSC. This shows that we can use Landsat T-O data to identify variation of water classes induced by changes in SSC in local water area.

### 4.3. SSCs are affected by interactions between currents and piers induced by the bridge

Changes of SSC on opposite sides of the bridge lead to differences in the water spectral profile curves in NIR band and further, to different water classes.

The temporal variation of SSC distribution in Hangzhou Bay is mainly caused by semidiurnal tide (Qiao et al., 2011). The tidal current, continuously changing its speed and direction during the tidal cycle, leads

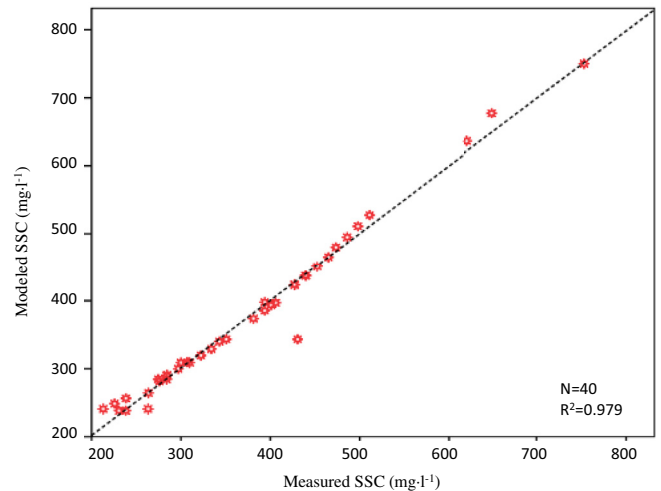


Fig. 6. Comparison of model estimated SSC and measured SSC. Matchup data were taken around the satellite data obtained time within 1 h.

the upstream and downstream sides of the bridge (HBB and JTB) to change. For example, the right side of the bridge in panel a (Fig. 4(B)) is upstream, while in panel b (Fig. 4(B)) is downstream and SSC distribution in the vicinity of the bridge changes (Figs. 4 and 5) accordingly.

In local area, SSC distribution in the vicinity of the bridge is influenced by the bridge obviously. The influence is mainly caused by the interaction of the currents with the bridge piers. The interaction induces hydrodynamic factors

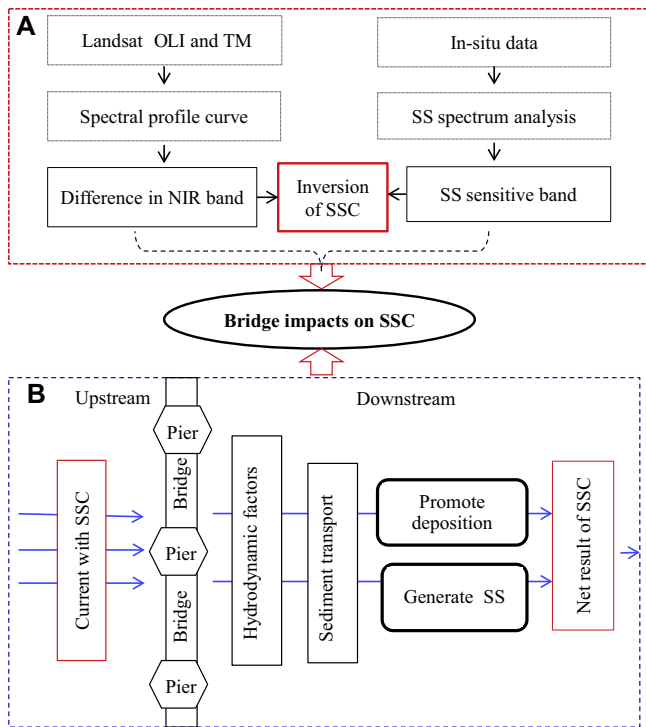


Fig. 7. Data analysis method (A) and the mechanism of effects of the bridge on SSC (B).

to change and influences suspended sediment transport (Baker, 1979; Pasiok and Stilger-SzydŁO, 2010; Unger and Hager, 2007).

Bridge piers can block currents (Liu, 2006; Pasiok and Stilger-SzydŁO, 2010) leading to decrease in current speed (Qiao et al., 2011) that promotes SS deposition. Meanwhile, bridge piers can also induce downward streams, which scour seabed nearby the base of the bridge piers and induce re-suspension of sediments. Therefore, the variation in SSC downstream is the net result of deposition and re-suspension. When re-suspension is greater than deposition, SSC increases; when re-suspension is less than deposition, SSC decreases; when re-suspension equals to deposition, SSC remains unchanged.

## 5. Conclusions

High spatial resolution Landsat T-O data can be used to investigate the impacts of a bay bridge on local water SSC. The analysis of spectral feature, model estimated SSC and unsupervised classification can display very well the SSC variations on the two sides of the bridge crossing Hangzhou Bay (Fig. 7(A)).

The results reveal that SSC changes significantly in the vicinity of the bridge. When there is low turbidity in upstream water, SSC tends to increase in downstream side; when there is high turbidity in upstream water, SSC tends to decrease in downstream water. The change of SSC on two sides of the bridge is the main factor that causes the differences in water masses.

The bay bridge affects SSC by interaction of currents and bridge's piers, leading to SS deposition and re-suspension downstream (Fig. 7(B)). These results can be generalized to other coastal engineering structures.

The mechanism of the bridge's impacts on SSC transport needs further study.

## Acknowledgments

This work is jointly supported by research projects awarded to DanLing Tang: (1) Key Project of National Natural Sciences Foundation of China (41430968); (2) Collaborative Innovation Center for 21st-Century Maritime Silk Road Studies, Guangzhou, China and Dragon 3 Project of ESA and NRSCC (10705, Tang & Alpers); (4) Inter-Governmental S&T Cooperation (China-Romania) (Tang & Laura); (3) 1-3-5 program of SCSIO, CAS. This work is also supported by research project of Zhejiang Department of Education (Y201225122). Institute of Remote Sensing and Digital Earth, Chinese Academy of Sciences, China provided Landsat TM and OLI data. Thanks for Dr. Gad Levy for his valuable comments and suggestions on this study.

## References

- Baban, S.M., 1997. Environmental monitoring of estuaries; estimating and mapping various environmental indicators in Breydon Water Estuary, UK, using Landsat TM imagery. *Estuarine Coastal Shelf Sci.* 44 (5), 589–598.
- Baker, C., 1979. The laminar horseshoe vortex. *J. Fluid Mech.* 95 (02), 347–367.
- Ball, G.H., Hall, D.J., 1965. ISODATA, a novel method of data analysis and pattern classification. DTIC Document.
- Bukata, R.P., Jerome, J.H., Bruton, J.E., 1988. Particulate concentrations in Lake St. Clair as recorded by a shipborne multispectral optical monitoring system. *Remote Sens. Environ.* 25, 201–229.
- Charou, E., Stefouli, M., Dimitrakopoulos, D., Vasiliou, E., Mavrantza, O.D., 2010. Using remote sensing to assess impact of mining activities on land and water resources. *Mine Water Environ.* 29 (1), 45–52.
- Chavez Jr, P.S., 1988. An improved dark-object subtraction technique for atmospheric scattering correction of multispectral data. *Remote Sens. Environ.* 24 (3), 459–479.
- Chen, S.L., Zhang, G., Yang, S., 2003. Temporal and spatial changes of suspended sediment concentration and resuspension in the Yangtze River estuary. *J. Geog. Sci.* 13 (4), 498–506.
- Chen, T., Li, P., Zhang, L., 2005. Estimating suspended sediment concentration in Yangtze River from Landsat-TM image estimating suspended sediment concentration in Yangtze River from Landsat-TM image. *Proc. SPIE* 6043, MIPPR: SAR and multispectral image processing. 6043, 604319-1-604319-6.
- Curran, P., Novo, E., 1988. The relationship between suspended sediment concentration and remotely sensed spectral radiance: a review. *J. Coastal Res.* 4 (3), 351–368.
- Dekker, A.G., Vos, R., Peters, S., 2002. Analytical algorithms for lake water TSM estimation for retrospective analyses of TM and SPOT sensor data. *Int. J. Remote Sens.* 23 (1), 15–35.
- Doxaran, D., Cherukuru, N., Lavender, S.J., 2006. Apparent and inherent optical properties of turbid estuarine waters: measurements, empirical quantification relationships, and modeling. *Appl. Opt.* 45 (10), 2310–2324.
- Doxaran, D., Froidefond, J.M., Lavender, S., Castaing, P., 2002. Spectral signature of highly turbid water application with SPOT data to

- quantify suspended particulate matter concentration. *Remote Sens. Environ.* 81 (1), 149–161.
- ENVI., 1997. ENVI User's Guide. Research Systems Inc, Chapter 1–10.
- Fan, H., Huang, H., Tang, J., 2007. Spectral signature of waters in Huanghe estuary and estimation of suspended sediment concentration from remote sensing data. *Geomatics Inf. Sci. Wuhan Univ.* 32 (7), 601–604.
- Hale, G.M., Querry, M.R., 1973. Optical constants of water in the 200-nm to 200-micrometer wavelength region. *Appl. Opt.* 12 (3), 555–563.
- Ilyina, T., Pohlmann, T., Lammel, G., Sündermann, J., 2006. A fate and transport ocean model for persistent organic pollutants and its application to the North Sea. *J. Mar. Syst.* 63 (1), 1–19.
- Irvin, B.J., Ventura, S.J., Slater, B.K., 1997. Fuzzy and isodata classification of landform elements from digital terrain data in Pleasant Valley. *Wisconsin Geoderma* 77 (2), 137–154.
- Lavender, S., Pinkerton, M., Moore, G., Aiken, J., Blondeau-Patissier, D., 2005. Modification to the atmospheric correction of SeaWiFS ocean color images over turbid waters. *Cont. Shelf Res.* 25 (4), 539–555.
- Lee, Z., Carder, K.L., Steward, R.G., Peacock, T.G., Davis, C.O., Mueller, J.L., 1996. Protocols for measurement of remote-sensing reflectance from clear to turbid waters. Presented at SeaWiFS Workshop, Halifax.
- Li, J., Gao, S., Wang, Y., 2010. Delineating suspended sediment concentration patterns in surface waters of the Changjiang Estuary by remote sensing analysis. *Acta Oceanologica Sin.* 29 (4), 38–47.
- Li, L., Jiang, Q., Zhang, L., Ding, G., Wang, L., Zhang, R., Zhang, Z.G., Li, Q., Ewing, J.R., Kapke, A., 2006. Ischemic cerebral tissue response to subventricular zone cell transplantation measured by iterative self-organizing data analysis technique algorithm. *J. Cerebral Blood Flow Metab.* 26 (11), 1366–1377.
- Lin, C.-M., Zhuo, H.-C., Gao, S., 2005. Sedimentary facies and evolution in the Qiantang River incised valley, Eastern China. *Mar. Geol.* 219 (4), 235–259.
- Liu, H., 2006. Hydrodynamic problems associated with construction of sea-crossing bridges. *J. Hydrodyn. Ser. B.* 18 (3), 13–18.
- Liu, S., Liu, Y., Yang, G., Qiao, S., Li, C., Zhu, Z., Shi, X., 2012. Distribution of major and trace elements in surface sediments of Hangzhou Bay in China. *Acta Oceanologica Sin.* 31 (4), 89–100.
- Lu, D., Mausel, P., Brondizio, E., Moran, E., 2002. Assessment of atmospheric correction methods for Landsat TM data applicable to Amazon basin LBA research. *Int. J. Remote Sens.* 23 (13), 2651–2671.
- Mayer, L.M., Keil, R.G., Macko, S.A., Joye, S.B., Ruttenberg, K.C., Aller, R.C., 1998. Importance of suspended particulates in riverine delivery of bioavailable nitrogen to coastal zones. *Global Biogeochem. Cycles* 12 (4), 573–579.
- Mobley, C.D., 1999. Estimation of the remote-sensing reflectance from above-surface measurements. *Appl. Opt.* 38 (36), 7442–7455.
- Mueller, J.L., Fargion, G.S., McClain, C.R., Mueller, J., Brown, S., Clark, D., Johnson, B., Yoon, H., Lykke, K. and Flora, S., 2003. Ocean Optics Protocols For Satellite Ocean Color Sensor Validation, Revision 5, Volume VI: Special Topics in Ocean Optics Protocols, Part 2. NASA Tech. Memo. 211621.
- Mustak, S., 2013. Correction of atmospheric haze in Resourcesat-1 LISS-4 MX data for urban analysis: an improved dark object subtraction approach International Archives of the Photogrammetry, Remote Sensing and Spatial Information Sciences. XL-1/W3, 5.
- Onderka, M., Pekárová, P., 2008. Retrieval of suspended particulate matter concentrations in the Danube River from Landsat ETM data. *Sci. Total Environ.* 397 (1), 238–243.
- Pasiok, R., Stilger-SzydŁo, E., 2010. Sediment particles and turbulent flow simulation around bridge piers. *Arch. Civil Mech. Eng.* 10 (2), 67–79.
- Qiao, S., Pan, D.I., He, X.Q., Cui, Q.F., 2011. Numerical study of the influence of Donghai Bridge on sediment transport in the mouth of Hangzhou Bay. *Proc. Environ. Sci.* 10 (2011), 408–413.
- Qiu, Z.F., 2013. A simple optical model to estimate suspended particulate matter in Yellow River Estuary. *Opt. Exp.* 21 (23), 27891–27904.
- Richter, R., 1990. A fast atmospheric correction algorithm applied to Landsat TM images. *Title Remote Sens.* 11 (1), 159–166.
- Shen, F., Verhoef, W., Zhou, Y., Salama, M.S., Liu, X., 2010. Satellite estimates of wide-range suspended sediment concentrations in Changjiang (Yangtze) estuary using MERIS data. *Estuaries Coasts* 33 (6), 1420–1429.
- Tang, D.L., Ni, I., Müller-Karger, F., Liu, Z., 1998. Analysis of annual and spatial patterns of CZCS-derived pigment concentration on the continental shelf of China. *Cont. Shelf Res.* 18 (12), 1493–1515.
- Tang, J., Tian, G., Wang, X.Y., Wang, X.M., Song, Q., 2004. The methods of water spectra measurement and analysis I: above water method. *J. Remote Sens.* 8 (1), 37–44.
- Teillet, P., Fedosejevs, G., 1995. On the dark target approach to atmospheric correction of remotely sensed data. *Can. J. Remote Sens.* 21 (4), 374–387.
- Ting, F.C., Briaud, J.-L., Chen, H., Gudavalli, R., Perugu, S., Wei, G., 2001. Flume tests for scour in clay at circular piers. *J. Hydraul. Eng.* 127 (11), 969–978.
- Tyagi, P., Bhosle, U., 2011. Atmospheric correction of remotely sensed images in spatial and transform domain. *Int. J. Image Processing (IJIP)* 5 (5), 564–579.
- Unger, J., Hager, W.H., 2007. Down-flow and horseshoe vortex characteristics of sediment embedded bridge piers. *Exp. Fluids* 42 (1), 1–19.
- Wang, F., Zhou, B., Liu, X., Zhou, G., Zhao, K., 2012. Remote-sensing inversion model of surface water suspended sediment concentration based on in situ measured spectrum in Hangzhou Bay, China. *Environ. Earth Sci.* 67 (6), 1669–1677.
- Webster, T., Lemckert, C., 2002. Sediment resuspension within a microtidal estuary/embayment and the implication to channel management. *J. Coastal Res.* 36, 753–759.
- Xie, D., Wang, Z., Gao, S., De Vriend, H., 2009. Modeling the tidal channel morphodynamics in a macro-tidal embayment, Hangzhou Bay, China. *Cont. Shelf Res.* 29 (15), 1757–1767.
- Yan, Z., Tang, D.L., 2009. Changes in suspended sediments associated with 2004 Indian Ocean tsunami. *Adv. Space Res.* 43 (1), 89–95.
- Zhang, M., Tang, J., Dong, Q., Song, Q., Ding, J., 2010. Retrieval of total suspended matter concentration in the Yellow and East China Seas from MODIS imagery. *Remote Sens. Environ.* 114 (2), 392–403.
- Zhang, M., Dong, Q., Cui, T., Xue, C., Zhang, S., 2014a. Suspended sediment monitoring and assessment for Yellow River estuary from Landsat TM and ETM+imagery. *Remote Sens. Environ.* 146, 136–147.
- Zhang, X.F., Hu, F., Zhang, J., Tang, D.L., 2014b. Northward drift of suspended sediment concentration in the Yangtze estuary in spring. *Int. J. Remote Sens.* 35 (11–12), 4114–4126.
- Zhou, W., Wang, S., Zhou, Y., Troy, A., 2006. Mapping the concentrations of total suspended matter in Lake Taihu, China, using Landsat-5 TM data. *Int. J. Remote Sens.* 27 (6), 1177–1191.